Impact of Microstructural Properties on Ionic and Heat Transport in NaSICON Glass Ceramics

Frank Tietz,* Philipp Odenwald, Doris Sebold, Mareen Schaller, Thorben Böger, Jan Köttgen, Qianli Ma, Sylvio Indris, Wolfgang G. Zeier, Oana Cojocaru-Mirédin, and Dina Fattakhova-Rohlfing

Two composition series of Zr-deficient NaSICON materials are investigated with respect to their ionic and thermal transport properties. The bulk conductivity varies between 1.4 and 6.6 mS cm^{-1}. The total conductivity showdecreasing values with increasing Zr deficiency due to the impact of the increasing fraction of glass phase. The calculated grain boundary conductivity is about two orders of magnitude lower than the total conductivity but does not correspond to the conductivity of any known glass composition of sodium silicates/phosphates. Nuclear magnetic resonance reveals three ^{23}Na relaxation rates, the fastest of which is attributed to the NaSICON phase and the two slower relaxation rates to sodium orthophosphates and the glass phase. Thermal conductivity varies between 0.9 and 1.0 W m^{-1} K^{-1} at 25 °C. At elevated temperatures, a clear trend is observed toward lower thermal conductivity with a higher glass fraction. In addition, atom probe tomography is applied to precisely quantify the composition of specific microstructural regions found within the glassy phase. A scanning electron microscopy study of the surfaces of sintered pellets shows an increasing amount of glass phase between the NaSICON particles with increasing Zr deficiency. Furthermore, a time-dependent phase separation is observed in relation to the dynamic formation and dissolution of Na$_3$PO$_4$ domains.

1. Introduction

Since the electrolyte is an indispensable and central part of batteries, the investigation and optimization of suitable liquid and solid electrolyte materials are crucial to the development of alkali-ion batteries and solid-state batteries, respectively. In the case of Na$^+$ ion conducting solid electrolytes, the β/β''-aluminas were predominant in the development stage, and high-temperature batteries with these electrolytes have already been commercialized.[1,2] At the same time, Na$^+$ superionic conductors (NaSICONs)[3,4] along

F. Tietz, P. Odenwald, D. Sebold, Q. Ma, D. Fattakhova-Rohlfing
Institute of Energy Materials and Devices
IMD-2: Materials Synthesis and Processing
Forschungszentrum Jülich GmbH
52425 Jülich, Germany
E-mail: f.tietz@fz-juelich.de

F. Tietz, D. Fattakhova-Rohlfing
Institute of Energy Materials and Devices
IMD-4: Helmholtz Institute Münster – Ionics in Energy Storage
Forschungszentrum Jülich GmbH
52425 Jülich, Germany

W. G. Zeier
Institute of Energy Materials and Devices
IMD-4: Helmholtz Institute Münster – Ionics in Energy Storage
Forschungszentrum Jülich GmbH
48149 Münster, Germany

P. Odenwald
Keysight Technologies Deutschland GmbH
Herrenberger Straße 130, 71034 Böblingen, Germany

M. Schaller, S. Indris
Institute for Applied Materials – Energy Storage Systems
Karlsruhe Institute of Technology
Hermann-von-Helmholtz-Platz 1, 76344 Eggenstein-Leopoldshafen, Germany

T. Böger, W. G. Zeier
Institute of Inorganic and Analytical Chemistry
University of Münster
Corrensstraße 28/30, 48149 Münster, Germany

T. Böger
International Graduate School for Battery Chemistry, Characterization, Analysis, Recycling and Application (BACCARA)
University of Münster
48149 Münster, Germany

J. Köttgen
I. Physical Institute (IA)
RWTH Aachen University
52056 Aachen, Germany

O. Cojocaru-Mirédin
Department of Sustainable Systems Engineering (INATECH)
University of Freiburg
Georges-Köhler-Allee 102, 79110 Freiburg, Germany

D. Fattakhova-Rohlfing
Faculty of Engineering and Center for Nanointegration Duisburg-Essen (CENIDE)
University of Duisburg-Essen
Lotharstraße 1, 47057 Duisburg, Germany

Batteries & Supercaps

Research Article
doi.org/10.1002/batt.202500093

Chemistry
Europe
European Chemical
Societies Publishing

the $Na_{1+u}Zr_2Si_uP_{3-u}O_{12}$ series have been studied intensively as well as compositions that deviate from this solid solution. In particular, Zr-deficient materials have been characterized. Examples can be found along the solid solutions $Na_{1+v}Zr_{2-v/3}Si_vP_{3-v}O_{12-2v/3}$,[5–10] $Na_3Zr_{2-w/4}Si_{2-w}P_{1+w}O_{12}$,[11,12] and $Na_{3.4}Zr_{2-y}Si_{2.4}P_{0.6}O_{12-2y}$.[13] It is also important to mention glasses, the so-called NaSIglas,[14] with the same compositions as the former solid solution[14,15] or mixtures of $Na_{1+u}Zr_2Si_uP_{3-u}O_{12}$ ceramics with sodium silicates as sintering additives,[16–18] since, in all these cases, the glass fraction plays an important role in the resulting effective properties of the materials.

The inspiration for investigating the two composition series of this work, $Na_{3.4}Zr_{2-3x/4}Si_{2.4-x/4}P_{0.6+x/4}O_{12-11x/8}$ (composition series 1, hereafter abbreviated as CS1) and $Na_{3.4}Zr_{2-3x/4}Si_{2.4+x/4}P_{0.6+1.5x/4}O_{12-x/16}$ (composition series 2, hereafter abbreviated as CS2) with $0 < x < 0.8$, is the work of von Alpen et al.[5] who reported high conductivity in the compound $Na_{3.1}Zr_{1.55}Si_{2.3}P_{0.7}O_{11}$, which meets the composition of the material in CS2 with $x = 0.4$. In subsequent publications,[6,7,9,10] the two-phase nature of this compound was explained, and it has been shown to have a high amount of glass phase together with a crystalline NaSICON phase. In this work, we systematically varied the Zr-deficiency and the polyanionic elemental distribution to gain a better understanding of the phase formation in this specific region of the phase diagram.[19] Since the second composition series has an ever-increasing proportion of silicate and phosphate and is not compensated for by the cation content, it is not surprising that an additional glass fraction forms. Therefore, the CS1 was defined for comparison, in which the anionic content is kept constant ($n_{Si} + n_P = 3$), which is common for NaSICON compounds and the variation of phase formation is dependent on the Zr deficiency.

In a previous publication, the chemistry of the crystalline phase was investigated in detail, particularly the impact of Zr deficiency in these NaSICON materials on phase formation, sinter ability, and crystallographic properties.[19] The two composition series previously mentioned also clearly demonstrated a vitreous phase progressively forming with increasing x, either as sodium silicate and/or as sodium phosphosilicate. The compounds with $x > 0.2$ therefore have to be regarded as glass-ceramic composites. The Rietveld refinement of neutron diffraction patterns revealed a nearly constant Zr deficiency of 2–4%, which was confirmed by quantitative energy-dispersive X-ray spectroscopy with slightly higher deficiencies (5–8%). After the in-depth analysis of the sintering products obtained after heat treatment at 1250 °C, the influence of the increasing glass fraction in the glass-ceramics on ionic and thermal conductivity is investigated here and combined with additional structural characterization methods. This is therefore the first systematic study on the transport properties of NaSICON glass ceramics. The relationship between morphological changes and transport properties provides us with important information for the optimization of powder production as well as guidelines for processing ion-selective membranes to be used in batteries and electrolyzers.

2. Results and Discussion

2.1. Ionic Conductivity

2.1.1. Impedance Spectroscopy

For the determination of the transport properties of the studied compositions, impedance spectra were measured between 20 and 100 °C. Two samples of CS2 with a high glass content ($x = 0.6$ and $x = 0.8$) were also measured down to −100 °C. The Nyquist plots of the impedance spectra at 25 °C are similar and shown in **Figure 1**a (CS1) and Figure S1, Supporting Information (CS2). Only one semicircle was observed for all specimens using a frequency range of 1 Hz to 3 MHz. At high frequencies, the left intercept with the x-axis did not coincide with the origin. The left intercept was therefore interpreted as the bulk resistance (R_b) and the semicircle as the response of the grain boundaries or glass phase. The right intercept with the x-axis was thus regarded as the total resistance (R_{total}) of the samples. At low frequencies, the straight line corresponded to the electrode polarization. The meaning of the different resistance contributions used in this work is summarized in **Table 1**. The radius of the semicircles increased with increasing x for both composition series, resulting in a continuously decreasing total conductivity (σ_{total}). Since the described determination of R_b is not very accurate, high-frequency measurements in the GHz range were
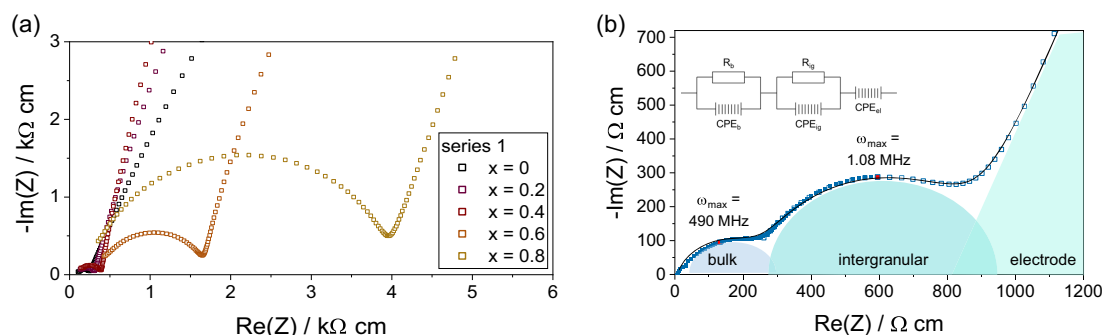

Figure 1. a) Normalized impedance spectra for CS1 recorded at 25 °C in the frequency range of 1 Hz–3 MHz. b) Normalized impedance spectrum composed of a high-frequency measurement (1 MHz–3 GHz; filled symbols) and a low-frequency measurement (1 Hz–3 MHz; open symbols). The solid line represents the result of the fitted spectrum with the equivalent circuit displayed at the top left. Here, the impedance of the $Na_{3.4}Zr_{1.7}Si_{2.5}P_{0.75}O_{11.98}$ sample (CS2, $x = 0.4$) is shown as an example. The slightly larger, red-filled data points correspond to the ω_{max} frequencies.

Table 1. Notation and meaning of the resistance (or conductivity) contributions. Capacitances and constant phase elements, as discussed below, are related to the contributions with the corresponding subscript designations.

Contribution	Explanation
R_b (σ_b)	Bulk resistance (conductivity) refers to the resistance (conductivity) of ionic transport in the grain interior
R_{gb} (σ_{gb})	Grain boundary resistance (conductivity) refers to the resistance (conductivity) of ionic transport in a polycrystalline material between individual grains with intimate contact
R_{glass} (σ_{glass})	Glass resistance (conductivity) refers to the resistance (conductivity) of ionic transport in the glass fraction and can also be understood as R_b of the glass fraction
R_{ig} (σ_{ig})	Sum of R_{gb} and R_{glass} of a crystalline/glass composite if the two contributions in the impedance spectra cannot be separated from each other
R_{total} (σ_{total})	Sum of R_b, R_{gb} and R_{glass}

performed. An additional semicircle can thus be recorded (Figure 1b), originating from the crystalline fraction of the samples, and is a direct observation of R_b.

R_b and the grain boundary resistance or—more appropriately in this case—the intergrain resistance including the glass phase ($R_{ig} = R_{gb} + R_{glass}$) can be derived from the fitting data of the impedance spectra. While σ_b can be calculated by the Equation (1)

$$\sigma_b = \frac{L}{A\,R_b} \qquad (1)$$

using the sample dimensions (L is the thickness of sintered pellets; A is the area of the electrodes), the conventional calculation of σ_{gb} requires the volume fraction of the grain boundaries derived from the capacitances of the individual transport contributions. The capacitances can be calculated from the data fitting of the impedance spectra according to Equation (2)

$$C = R^{\frac{1-n}{n}} C_{CPE}^{1/n} \qquad (2)$$

where R, C_{CPE}, and n are the fitted equivalent circuit parameters, that is, the resistance, the capacitance of the constant phase element and its exponent, respectively, of the bulk or the grain-boundary contribution. In the brick-layer model, the ratio of the capacitances, C_b/C_{gb}, is regarded as the overall volume fraction of grain boundaries in the sample, assuming that both bulk and grain boundaries have the same dielectric constants.[20,21] σ_{gb} can then be calculated with the grain boundary resistance ($R_{gb} = R_{total} - R_b$).

$$\sigma_{gb} = \frac{L}{A} \left(\frac{C_b}{C_{gb}} \right) \frac{1}{R_{gb}} \qquad (3)$$

In samples with a high glass fraction, Equation (3) is also used, as the impedance spectra did not clearly show a separate semicircle of the glass, that is, R_{gb} and R_{glass} seem to have similar characteristic frequencies. As a result, $R_{gb} \hat{=} R_{ig}$ and $\sigma_{gb} \hat{=} \sigma_{ig}$, and σ_{ig} comprise all transport processes outside the NaSICON grains.

The capacitance associated with the high-frequency arc is found to vary between 10^{-11} and 10^{-13} F, and the one associated with the lower frequency arc is between 10^{-9} and 10^{-10} F for all samples.

All samples for conductivity measurements had a relative density of >93%. Only the samples with the composition $Na_{3.4}Zr_{1.4}Si_{2.6}P_{0.9}O_{11.95}$ (CS2, $x = 0.8$) showed densities between 83% and 91% (higher densities were obtained at lower sintering temperatures, see discussion below). For $Na_{3.4}Zr_{2}Si_{2.4}P_{0.6}O_{12}$, the various impedance measurements carried out between 2022 and 2024 resulted in a σ_{total} of 2 ± 1 mS cm^{-1}. The samples with $x = 0.2$ and $x = 0.4$ also showed total conductivities of more than 1 mS cm^{-1} for both composition series (**Figure 2**). The end members of the two composition series ($x = 0.8$), $Na_{3.4}Zr_{1.4}Si_{2.2}P_{0.8}O_{10.9}$ and $Na_{3.4}Zr_{1.4}Si_{2.6}P_{0.9}O_{11.95}$, still had a surprisingly high σ_{total} of 0.36 and 0.2 mS cm^{-1}, respectively, considering the high proportion of glass phase in these samples.

The σ_{bulk} values followed a similar trend to σ_{total}, especially in the case of CS2 (see Figure 2). While for CS1, the σ_{bulk} remained nearly constant and varied only between 6.6 mS cm^{-1} ($x = 0$) and 3.7 mS cm^{-1} ($x = 0.4$), CS2 showed a steady decrease of σ_{bulk} from 6.2 mS cm^{-1} ($x = 0.2$) to 1.4 mS cm^{-1} ($x = 0.8$). The grain boundary conductivity calculated with Equation (2) and (3) resulted in values between 0.0041 and 0.005 mS cm^{-1}, with a generally smooth decreasing trend from $x = 0$ to $x = 0.8$ (Figure 2). Since this contribution to the total conductivity should also contain the conductivity of the glass phase, the data are significantly higher than the ionic conductivity of individual glass compositions (see discussion below). In terms of a two-phase composite, this means that the high conductive phase can form a sufficient number of conductive paths and thus a slightly decreased conductivity is maintained according to general effective media theory.[22,23] The theoretical data are in good agreement with the measured σ_{total} values (see Figure S2, Supporting Information), which suggests that the impact of the low-conducting glass phase, that is, the expected decrease of conductivity by several orders of magnitude, occurs at a percolation threshold of the
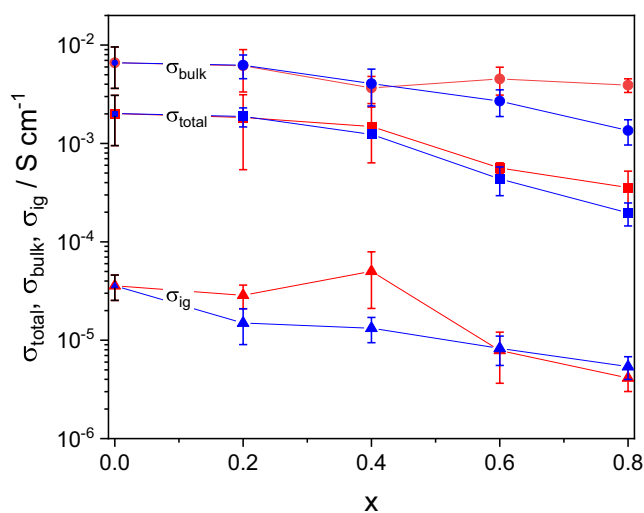

Figure 2. σ_{total}, σ_{bulk}, and σ_{ig} as a function of the stoichiometry parameter x in CS1 (red symbols) and CS2 (blue symbols). The error bars indicate the standard deviation of several measurements.
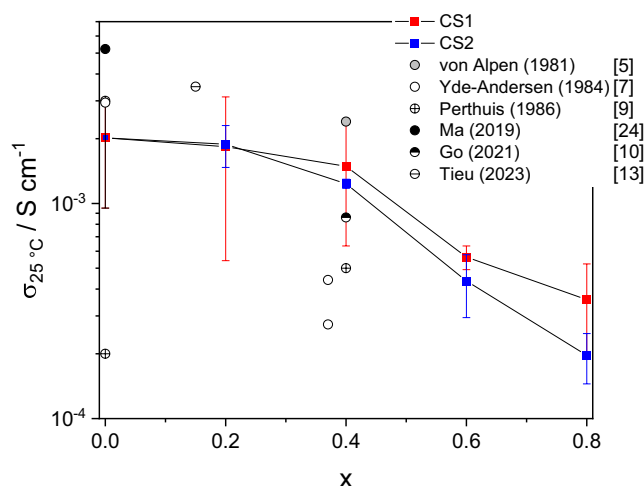
Figure 3. Comparison of σ_{total} with previously reported data. Here, x denotes the stoichiometry parameter x in CS1 and CS2 as well as the Zr deficiency of deviating compositions[5,7,9,10] after normalization to 3.4 mol Na/formula unit.

crystalline NaSICON volume fraction of about 40–50%. This is a much lower volume fraction than the lowest observed volume fraction of NaSICON in the investigated samples (about 65%[19]).

The obtained σ_{total} values are in good agreement with previous investigations (**Figure 3**). The high conductivity of 2.4 mS cm^{-1} reported for the Na$_{3.1}$Zr$_{1.55}$Si$_{2.3}$P$_{0.7}$O$_{11}$[5] compound could only be reproduced in a single measurement with the composition Na$_{3.4}$Zr$_{1.7}$Si$_{2.3}$P$_{0.7}$O$_{11.45}$ (CS2, $x = 0.4$). Lower values were otherwise measured. A comparison with the other data suffers from the fact that different sintering temperatures were often applied, leading to a varying density and crystallinity. The data of Yde-Anderson et al.[7] were obtained with the composition Na$_{3.25}$Zr$_{1.65}$Si$_{2.43}$P$_{0.89}$O$_{12}$ sintered at 1100 °C (for 9 h) and 1200 °C (for 3 h), resulting in nearly the same density. In the case of Na$_{3.4}$Zr$_2$Si$_{2.4}$P$_{0.6}$O$_{12}$, the sample was pressed with a pressure of

60 MPa before sintering at 1200 °C, resulting in nearly 100% relative density and an ionic conductivity of 2.94 mS cm^{-1}. This value was only surpassed recently.[24] Perthuis and Colomban[9] only sintered the Na$_{3.1}$Zr$_{1.55}$Si$_{2.3}$P$_{0.7}$O$_{11}$ compound at 1090 °C as well as Na$_3$Zr$_2$Si$_2$PO$_{12}$—although this composition has a lower sodium content and is not directly comparable with the other compositions—at 1050 and 1250 °C, demonstrating the wide conductivity range that can result from the sintering conditions. Similarly, Go et al.[10] treated Na$_{3.1}$Zr$_{1.55}$Si$_{2.3}$P$_{0.7}$O$_{11}$ with a pressure of 60 MPa for pellet compaction and sintering at 1200 °C for 1 h. A relative density of 98% was obtained and a σ_{total} value of 0.86 mS cm^{-1}, which falls into the regime of conductivities observed for $x = 0.4$ of CS1. Since the sintering temperature has a significant influence on the relative density, on phase formation, and, ultimately, on ionic conductivity, this interrelation was investigated for both composition series. In general, the increase of the glass phase leads to earlier densification (at lower sintering temperature),[19] but σ_{total} values >1 mS cm^{-1} are only observed after sintering at temperatures higher than 1200 °C[7,9,13,24] (see Figure S3, Supporting Information, with the dependence of relative density and σ_{total} on sintering temperature for CS1).

The temperature dependence of the ionic conductivity was measured for all samples between 20 and 100 °C. For the samples of CS2 with $x = 0.6$ and $x = 0.8$, the temperature interval was extended down to −100 °C (**Figure 4**a) to determine the possible influences of the glass content, for example, a higher activation energy at low temperatures. A more detailed view of the high temperature region is shown in Figure S4, Supporting Information. From the slope of the curves, the activation energies were determined using the Arrhenius equation and showed very similar values between 0.27 and 0.32 eV. Only the Na$_{3.4}$Zr$_{1.85}$Si$_{2.35}$P$_{0.65}$O$_{11.03}$ sample ($x = 0.2$, CS1) with the lowest amount of glass fraction and smallest particle sizes[19] showed a lower activation energy (E_a) of 0.21 eV (**Table 2**). In general, the activation energies increased with an increasing glass fraction
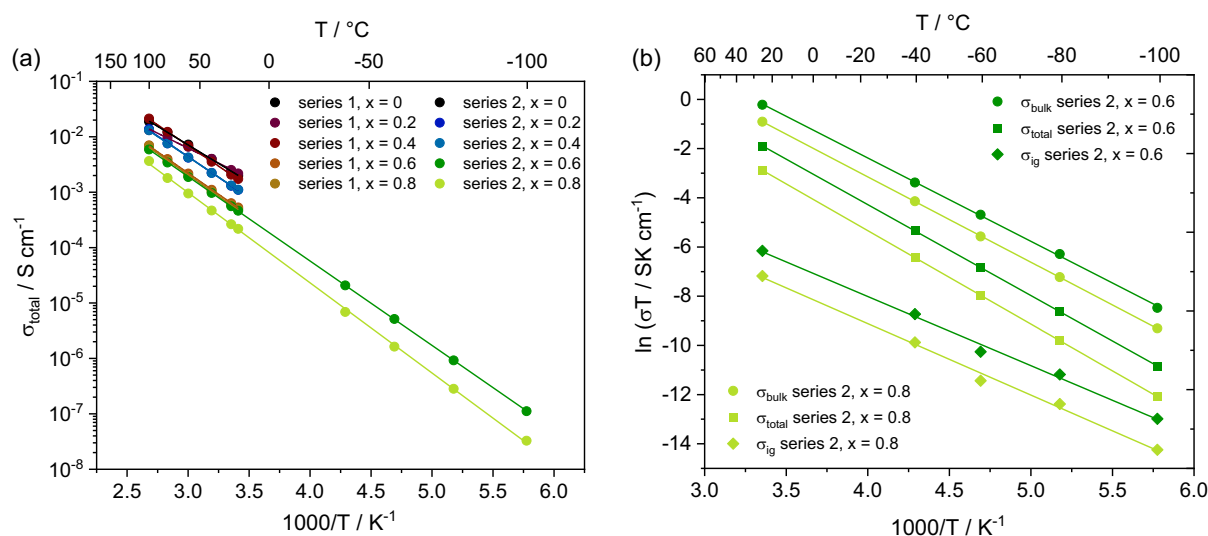

Figure 4. a) Temperature-dependent measurements in the temperature range of −100–100 °C. b) Low-temperature data between 20 °C and −100 °C for the samples of CS2 with the highest glass content ($x = 0.6$ and $x = 0.8$). Very noteworthy, the slope of σ_{ig} is significantly lower than those of σ_{bulk} and σ_{total}.

Batteries & Supercaps

Research Article
doi.org/10.1002/batt.202500093

Chemistry Europe
European Chemical
Societies Publishing

Table 2. Glass fraction,[19] activation energy, and ionic conductivity at room temperature, as shown in Figure 4.

Composition series	x	Glass fraction [%]	$E_a(\sigma_{total})$ [eV]	σ_{total} [mS cm^{-1}]	$E_a(\sigma_{bulk})$ [eV]	$E_a(\sigma_{ig})$ [eV]
1 + 2	0	10	0.266 ± 0.002	2.37	–	–
1	0.2	9	0.214 ± 0.006	3.41	–	–
1	0.4	19	0.296 ± 0.002	2.06	–	–
1	0.6	27	0.304 ± 0.003	0.63	–	–
1	0.8	26	0.306 ± 0.006	0.59	–	–
2	0.2	8	0.296 ± 0.005	1.30	–	–
2	0.4	19	0.291 ± 0.003	1.32	–	–
2	0.6	28	0.302 ± 0.001	0.50	0.292 ± 0.003	0.24 ± 0.01
2	0.8	35	0.323 ± 0.002	0.19	0.299 ± 0.001	0.25 ± 0.01

(Table 2). In the case of the low-temperature measurements of the two samples of CS2, the activation energies of σ_{total}, σ_{bulk}, and σ_{ig} were determined by applying Equation (2) and (3) (Figure 4b). While the E_a of σ_{bulk} is only a few percentage points lower than that of σ_{total}, it is interesting to note that the smaller slope of σ_{ig} indicates a significantly lower E_a of σ_{ig}, which is 0.06–0.07 eV less than that of σ_{total}.

The determined activation energies of σ_{total} are in very good agreement with many previous measurements on various NaSICON materials. In **Figure 5**, a compilation of temperature-dependent ionic conductivities of Zr-deficient NaSICON materials is displayed. The obtained data in Figure 4b and S2, Supporting Information are depicted here by a green trapezoid, and the upper and lower limits have comparable slopes to many other materials.

While the decrease in conductivity with increasing glass content is not surprising and can be explained by the percolation theory as discussed above and visualized in Figure S2, Supporting Information, there are still other aspects that need to be considered in more detail. If the C_b/C_{gb} ratio is regarded as the overall volume fraction of grain boundaries in the sample, the calculated values are about one order of magnitude lower than the observed glass fractions. In other words, the brick-layer model does not correctly describe the observed microstructures with a high volume fraction of the glass. As an alternative, samples with a high glass fraction can also be treated as a two-phase material, in which both components contribute with two jump frequencies (Figure 1b) and the two semicircles are directly related to the two phases. When the conductivity of the glass fraction is determined from R_{total} as $R_{glass} = R_{total} - R_{bulk}$, the resulting values would thus be even higher than those considering the brick-layer model (between σ_{bulk} and σ_{total} in Figure 2). In addition, the calculated "grain-boundary conductivities" are, as expected, significantly lower than the total conductivities, but the calculations of σ_{ig} indicate that the intergrain conductivity is two to four orders of magnitude higher than the conductivity of well-characterized glasses of sodium silicates or sodium phosphates (see Figure S5, Supporting Information). In the case of the hypothetical σ_{glass}, as outlined above, the difference would increase by two additional orders of magnitude.

Aside from percolation theory (Figure S2, Supporting Information), there might be another transport mechanism which has not been considered so far. At sintering temperatures above 1200 °C, there is a substantial weight loss due to Na$_2$O evaporation.[29,30] The small, nm-sized tubular porosity that can be seen in scanning electron microscopy (SEM) images with high magnification (see Figure 11a and 12a in Section 2.3.1 and SEM images in ref. [19]) is regarded as the transport path of Na$_2$O depletion and the reason for the density decrease during sintering, since the Na$_2$O gas diffuses through these little channels towards larger spherical pores. It is likely that the surface of these pores is covered by sodium species (and/or concentration gradients in the glass phase) after sintering, which may contribute to the total conductivity in the form of surface diffusion along the pores. What is so far just a hypothesis, this conduction mechanism requires a more systematic investigation on the existing samples or with a model system, but the atom probe tomography (ATP) investigations shown below strongly support this scenario.
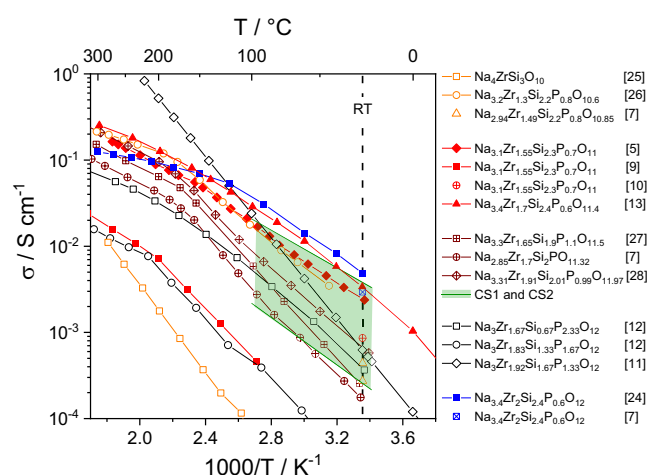

Figure 5. Compilation of total ionic conductivities of various Zr-deficient NaSICON materials. The orange symbols show the conductivities of materials with a very low Zr content,[25,26] the red symbols represent the conductivities of the "von Alpen composition," the brown symbols indicate various other compositions with $n_{Si}/n_p \approx 2$,[27,28] the black symbols depict the compositions with a constant Na content of 3 mol/formula unit, and, for comparison, the blue symbols represent the data of the Na$_{3.4}$Zr$_2$Si$_{2.4}$P$_{0.6}$O$_{12}$ composition without Zr deficiency. The light green area represents the measured data range shown in Figure 4a and S4, Supporting Information.

2.1.2. NMR

^{23}Na, ^{29}Si, and ^{31}P magic-angle spinning (MAS) nuclear magnetic resonance (NMR) spectra were recorded to probe the local

environment around these nuclei at room temperature. The ^{29}Si spectra (Figure S6a, Supporting Information) show one resonance at −88 ppm, which can be attributed to the [SiO$_4$] tetrahedra.[31] For increasing x, the full width at half maximum (FWHM) of the peaks broadens from 3.1 to 3.3 ppm for CS1 and to 3.5 ppm for CS2 (see Figure S6c, Supporting Information). This broadening can be attributed to the higher glass fraction. Taking the position of ≈−86 to −92 ppm and assuming predominantly sodium silicate glasses,[19] the signal broadening in the ^{29}Si spectra can be attributed to the Si(Q_3) tetrahedra, and the sodium content can be estimated as 30–40 mol% Na$_2$O.[32] For the ^{23}Na spectra, the trend is less obvious. Since ^{23}Na (nuclear spin $I = 3/2$, nuclear quadrupolar moment $Q = 100.6$ mb)[33] experiences also quadrupolar interactions of the nuclear quadrupolar moment with electric field gradients being present at the site of the nucleus, variation in the local [NaO$_6$] octahedra can also lead to narrower signals, if these octahedra become, on average, more symmetric. This might cause the ^{23}Na NMR linewidth of series 2 to be almost constant for $x > 0.2$.

^{31}P MAS NMR spectra display a signal at ≈−10 ppm for all samples (**Figure 6**). This signal corresponds to [PO$_4$] tetrahedra[31] and broadens for increasing x similar to the ^{29}Si MAS NMR spectra. However, in contrast to the ^{29}Si signals, the broadening of the ^{31}P MAS spectra cannot be attributed to P(Q_n) tetrahedra observed for Na—(Si—)P—O glasses.[34] Only the very small signal at 2.5 ppm may be interpreted as a signal of P(Q_1) tetrahedra.[34] It can therefore be assumed that the glass fraction contains only a very low amount of phosphate. Additional signals at 7.2 and 14 ppm are
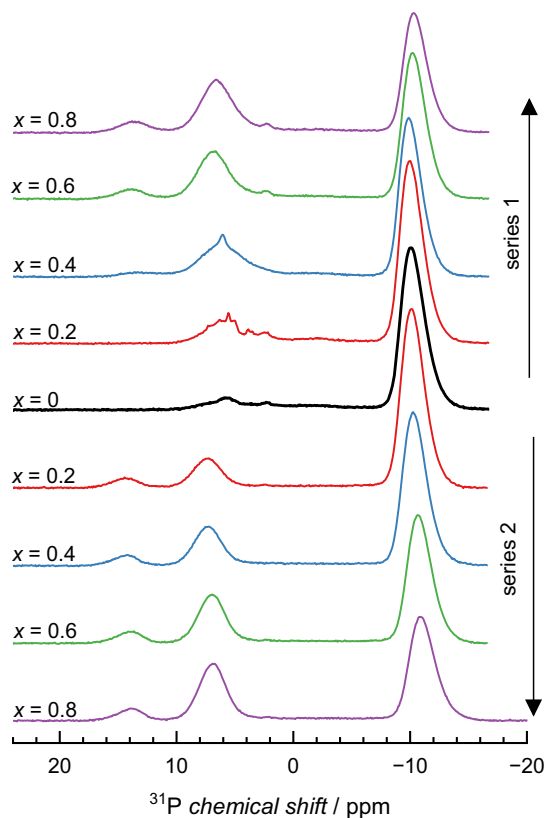
attributed to Na$_3$PO$_4$·12H$_2$O and Na$_3$PO$_4$, respectively.[35–37] A corresponding phase analysis by X-ray diffraction confirmed additional reflections of the two phosphates on samples that were exposed to ambient air for more than 1000 h (see Figure S7, Supporting Information, and Section 2.3.2).

^{23}Na spectra reveal one major peak at around −5.4 ppm (see Figure S6b, Supporting Information). The fast motions of the sodium ions in the crystalline phase cause a motionally averaged resonance even if different sodium positions are present in the crystalline structure. However, this peak also broadens for increasing x values from 10.7 to 15.2 and 12.7 ppm for CS1 and CS2, respectively, due to the increasing glass content and the associated slower motion of the Na$^+$ ions in this glass phase. The motion of the sodium ions can be investigated with static ^{23}Na relaxometry, the results of which are presented below. A small resonance at ≈7 ppm is also detected in the ^{23}Na MAS NMR spectra of CS1, which can be attributed to Na$_2$O$_2$ filaments,[35,38] as discussed above (see also Section 2.3.1).

Spin–lattice relaxation times are sensitive to motions in the order of the inverse Larmor frequency ω_L ($\tau \approx 1/52.9$ MHz ≈ 20 ns). ^{23}Na relaxometry and static line shape analysis are therefore well suited to study the local ion "hopping" motion from one crystallographic site to another. The temperature dependence of the inverse spin–lattice relaxation time can be described by the Bloembergen–Purcell–Pound (BPP) theory:[39,40]

$$T_1^{-1} \sim \left(\frac{\tau}{1 + \omega_L^2 \tau^2} + \frac{4\tau}{1 + 4\omega_L^2 \tau^2} \right) \tag{4}$$

assuming an isotropic, uncorrelated motion of the Na$^+$ ions. The correlation time τ can be described by an Arrhenius-type temperature dependence

$$\tau = \tau_0 \cdot \exp\left(\frac{E_a}{k_B T} \right) \tag{5}$$

where E_a is the activation energy, k_B is the Boltzmann constant, and T is the temperature. The temperature-dependent relaxation rates T_1^{-1} are displayed in **Figure 7**. For all samples, at least two distinctly different T_1 relaxation times were detected from the magnetization transients for low temperatures (see Figure S8, Supporting Information), indicating that the sodium ions reside in at least two different regions/phases where the ions diffuse with varying local motions. For $x = 0$ and $x = 0.2$ (both composition series), two different local motions are detected, whereas for higher x values, three motions can be observed for both composition series. In all cases, the majority component represents the fastest motion corresponding to the highest relaxation rate values (filled squares in Figure 7). These local motions are attributed to the crystalline phase, where the fraction decreases with increasing x. The signal fractions are given in **Table 3**. The lower relaxation rates correspond to the Na$_3$PO$_4$·12H$_2$O and Na$_3$PO$_4$ signals observed in the ^{31}P MAS NMR spectra. For $x = 0.2$ in CS1, only two relaxation times are determined, whereas three signals are detected in the ^{31}P MAS spectrum. This deviation could be explained by the different storage time of the sample at ambient conditions between both sets of experiments (see Section 2.3.2). At higher temperatures, only one relaxation rate is detected, revealing that all sodium ions now contribute
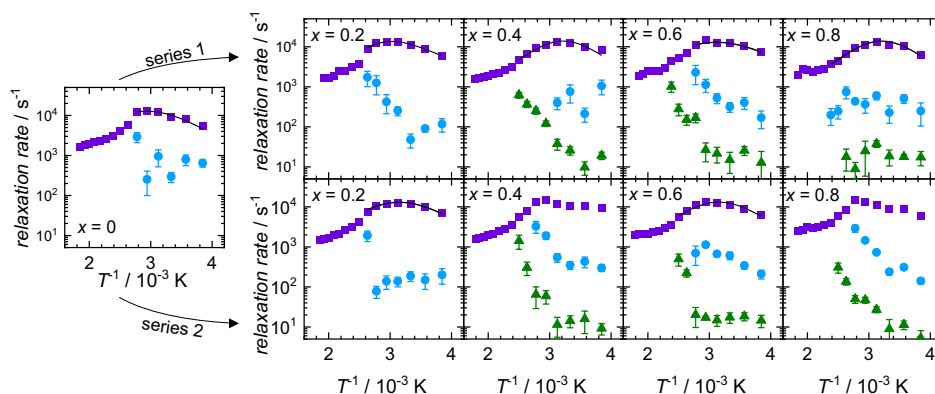

Figure 6. ^{31}P MAS NMR spectra of the samples.

Batteries & Supercaps

Research Article
doi.org/10.1002/batt.202500093

Chemistry Europe
European Chemical
Societies Publishing

Figure 7. ^{23}Na relaxation rates T_1^{-1} versus inverse temperature. Top: results for CS1, bottom: results for CS2. Filled squares: crystalline phase. Filled circles: Na$_3$PO$_4$·12H$_2$O. Filled triangles: Na$_3$PO$_4$.

Table 3. Activation energies were determined from the temperature-dependent T_1 measurements using Equation (4), and the NaSICON and sodium phosphate fractions were determined from the magnetization transients.

Composition series	x	E_a [eV]	NaSICON fraction [%]	Na$_3$PO$_4$·12H$_2$O fraction [%]	Na$_3$PO$_4$ fraction [%]
1 + 2	0	0.17 ± 0.02	86	14	–
1	0.2	0.17 ± 0.02	86	14	–
1	0.4	0.22 ± 0.02	73	14	13
1	0.6	0.15 ± 0.02	67	22	11
1	0.8	0.22 ± 0.02	60	24	16
2	0.2	0.17 ± 0.02	87	13	–
2	0.4	–	70	23	7
2	0.6	0.20 ± 0.02	65	25	10
2	0.8	–	50	38	12

to the long-range diffusion process and thus lower the overall ion diffusivity within the samples, especially in those with a small crystalline fraction.

The E_a of the local hopping motion in the crystalline region at low temperatures can be determined by the BPP theory using Equation (4). The results, listed in Table 3, reveal only little changes in the activation energies in both composition series. It is worth noting that it is not possible to apply the BPP theory to the samples with $x = 0.4$ and $x = 0.8$ in CS2, since the maximum of the relaxation rate is not clearly resolved. The determined activation energies are ≈0.1 eV lower than $E_a(\sigma_{total})$ derived by impedance spectroscopy. Since the NMR relaxometry only measures the local hopping motion of the sodium ions, the effects of grain boundaries or other defects in the crystalline phase, which possibly limit the motion of the sodium ions, are not detected here. Additionally, impedance spectroscopy probes the local and the long-range transport of the material, and a higher activation energy is therefore expected.

The ionic conductivity can also be estimated from the NMR results using the Einstein–Smoluchowski equation[41,42] and equation and the Nernst–Einstein equation

$$D = l^2/6\tau \tag{6}$$

with τ given by Equation (5), the hopping distance l, and the diffusion coefficient D

$$D = \sigma_{NMR} k_B T / N_{Na} q_{Na}^2 \tag{7}$$

where σ_{NMR} is the ionic conductivity, N_{Na} the charge carrier concentration, and q_{Na} the charge of the sodium ions. For the estimation of σ_{NMR}, an average hopping distance of 3.2 Å and a particle concentration of 14 ions per 1096.37 Å^3 were used, both of which were determined from the Rietveld refinements.[19] The room temperature ionic conductivities estimated from NMR and the σ_{bulk} values determined by impedance spectroscopy (see Figure 2) are plotted together in **Figure 8**. Here, the ionic conductivities are more reasonably correlated with the Na content in the crystalline phase, since the analytical compositions of the crystalline NaSICON phase do not correspond to the nominal compositions.[19] For this purpose, the compositions after refinement of the neutron diffraction data were used,[19] and the Na content was reduced by the amount of Zr deficiency (vacant Zr sites occupied by Na$^+$ ions) to obtain the amount of Na$^+$ ions in the conduction paths. These values were used to plot σ_{bulk} and σ_{NMR} versus the Na content (Figure 8). The absolute conductivity values are approximately only half of those reported for materials without Zr deficiency,[24] which might be partly attributed to the electrostatic forces caused by the occupation of Zr sites with Na$^+$ ions. However, the shape and maximum of the fitting curve, shown as a dashed line, are in very good agreement with the σ_{bulk} values previously determined.[24]
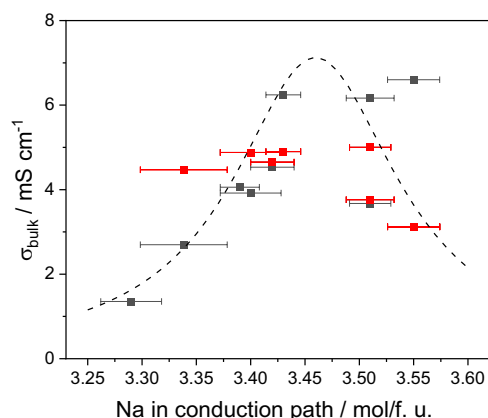
Figure 8. Room temperature ionic conductivity σ_{NMR} (red symbols) estimated from ^{23}Na relaxometry and σ_{bulk} (black symbols) determined by impedance spectroscopy as a function of the Na content in the conduction paths. The dashed line is a fitted curve (inverse polynomial, $y = 1/(197679 - 114196x + 16504x^2)$), which serves as a visual guide.

Motions in the range of milliseconds can be observed by temperature-dependent static line shape analysis of ^{23}Na NMR spectra. At low temperatures, the static spectra display broad line shapes. The faster motions at elevated temperatures cause a motional narrowing, where the lines become narrower with increasing temperature, as shown exemplarily on the temperature-dependent ^{23}Na NMR spectra of sample $x = 0.6$ of CS2 in Figure S9, Supporting Information. The FWHM of the ^{23}Na spectra allows for a comparison of the diffusive motions in the millisecond regime (see **Figure 9**b). The motional narrowing regime of the FWHM form is reached at similar temperatures for all samples. The higher plateau value of FWHM at low temperatures for increasing x is caused by the presence of the higher glass fraction. As shown in Figure 9a, the crystalline NaSICON and the sodium phosphate phase have different chemical shifts, resulting in broader spectra and, therefore, a larger FWHM.

2.2. Thermal Conductivity

Crystalline and glassy materials exhibit fundamentally different temperature dependences for their thermal conductivity. In crystalline materials, a maximum in the thermal conductivity is observed at very low temperatures (typically <50 K), known as the phonon peak, followed by a decrease in thermal conductivity with T^{-1}.[43] In contrast, in amorphous materials, the thermal conductivity increases monotonically and saturates at high temperatures. Glasses mostly exhibit a significantly lower thermal conductivity than crystals.[43]

The measured thermal conductivities reveal a trend toward lower thermal conductivities at high temperatures with an increasing glass fraction (**Figure 10**). At lower temperatures, this effect becomes less pronounced. It is not possible to draw quantitative conclusions due to a convolution of the slightly different compositions, varying sodium contents in the intergranular domains as well as the differing morphology of crystalline and glassy domains (see Section 2.3.1 and 2.3.2), and the unknown thermal conductivities of the purely glassy and purely crystalline phase. Qualitatively, however, the observed trend is as expected, given the generally lower thermal conductivity of glasses
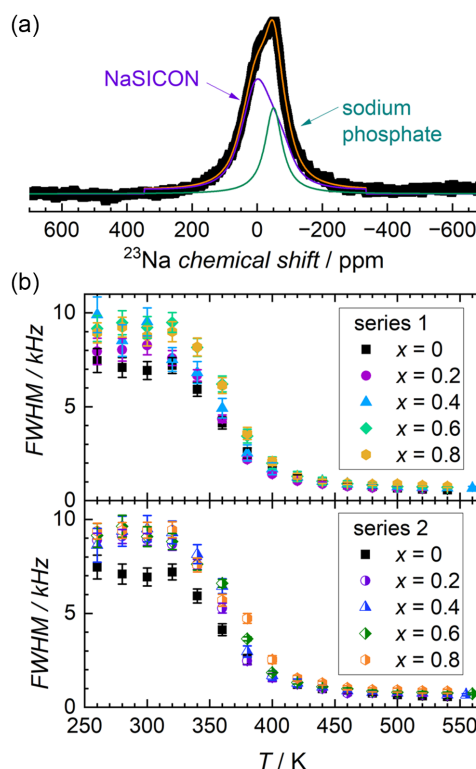

Figure 9. a) Static ^{23}Na spectrum of sample $x = 0.6$ of CS2 at 340 K, deconvoluted into the crystalline and sodium phosphate fraction. b) Temperature-dependent FWHM of CS1 (top) and CS2 (bottom).

compared to crystalline phases. In all compounds, the minimum thermal conductivity can be found between temperatures of 100 and 150 °C, with values ranging from 0.85 to 0.95 W m^{-1} K^{-1}. At -50 and 500 °C, the data vary between 0.9 and 1.02 W m^{-1} K^{-1} and between 0.9 and 1.13 W m^{-1} K^{-1}, respectively. The low magnitude of the thermal conductivity is in line with thermal conductivities reported previously on other Li$^+$ and Na$^+$ solid electrolytes[44–46] and other NaSICON materials.[47,48]

2.3. Microstructure

2.3.1. APT

The atom probe tomography (APT) results obtained on the samples Na$_{3.4}$Zr$_2$Si$_{2.4}$P$_{0.6}$O$_{12}$ (CS1 + 2, $x = 0$), Na$_{3.4}$Zr$_{1.4}$Si$_{2.2}$P$_{0.8}$O$_{10.9}$ (CS1, $x = 0.8$), and Na$_{3.4}$Zr$_{1.4}$Si$_{2.6}$P$_{0.9}$O$_{11.95}$ (CS2, $x = 0.8$) are summarized in **Figure 11**, **12**, and S10, Supporting Information. These figures cover two important aspects: the composition along the investigated region-of-interest provided by the 1D concentration profile (elemental composition per slice of 0.2 nm thickness) and proximity histograms as well as the 3D reconstruction maps. The proximity histograms, or proxigrams, are, in fact, 1D concentration profiles calculated from the starting point (0 nm position), which is represented by the iso-surface (triangulated surface of constant concentration value). The minimum distance of each ion from the chosen iso-surface is then calculated, which allows each ion to be assigned to a certain distance of the proximity histogram. Further details can be found in Keutgen et al.[49]
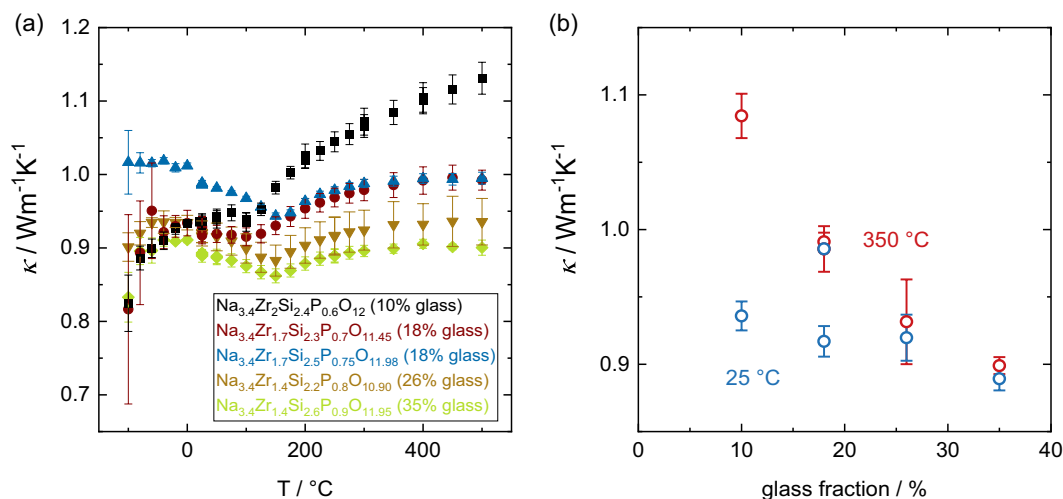
Batteries & Supercaps

Research Article
doi.org/10.1002/batt.202500093

Chemistry Europe
European Chemical
Societies Publishing

Figure 10. a) Thermal conductivities of NaSICON glass ceramics with different glass fractions. A trend toward lower thermal conductivity with higher glass fraction can be observed. b) Thermal conductivity at room temperature (blue circles) and 350 °C (red circles) plotted against the glass fraction. At 350 °C, a clear trend can be observed, which is not seen at room temperature.
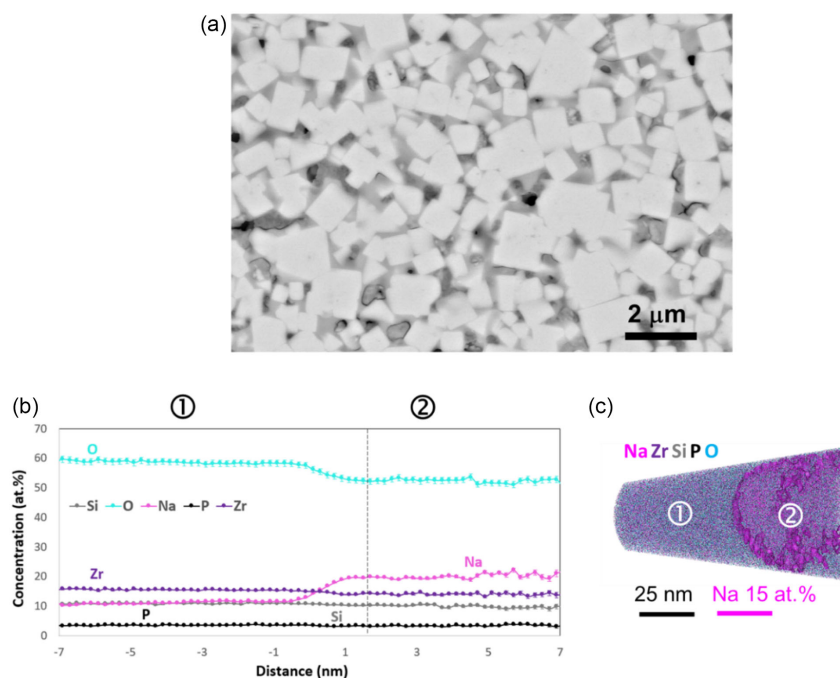

Figure 11. a) High-resolution SEM using BSEs. b,c) APT results obtained on the $Na_{3.4}Zr_{1.4}Si_{2.2}P_{0.8}O_{10.9}$ (CS1, $x = 0.8$) sample. Proximity histogram (in (b)) was constructed with an iso-surface built using a 15 at% Na isopleth value. The position 0 nm provides the location of the iso-surface. (c) 3D atom probe map exhibiting the Na redistribution (in pink) in the investigated regions where a Na-rich region (denoted by ②) can be clearly identified.

The Na ions were homogeneously distributed in the $Na_{3.4}Zr_2Si_{2.4}P_{0.6}O_{12}$ sample (see 3D APT map shown in Figure S10a, Supporting Information), whereas the other two samples surprisingly revealed an inhomogeneous Na distribution (Figure 11, 12, and S10, Supporting Information). All of the 3D maps of these two samples showed elongated cylindrical features enriched in Na (numbered as ②) along the cross section.

The composition values of the three samples, which were determined in regions ① and ②, are provided in **Table 4**. The O composition in region ① decreases while going from the reference sample with $x = 0$ to both end members with $x = 0.8$, with

an average concentration of 61.2 ± 0.5 at% ($x = 0$), 59.4 ± 0.5 at% (CS1, $x = 0.8$), and 57 ± 0.5 at% (CS2, $x = 0.8$). Interestingly, the opposite trend was observed for Na with 7.7 ± 0.3, 11.5 ± 0.3, and 14.75 ± 0.3 at%, respectively. However, these Na composition values are well below the expected nominal composition value varying between 16.6 and 18.8 at%. This clearly confirms that Na-rich regions are formed in both samples with $x = 0.8$.

Moreover, the average Na composition in region ② also increases from 28.1 ± 0.3 to 33.65 ± 0.3 at% in comparison to the results of the samples with $x = 0.8$ when going from CS1 to CS2. This suggests that increasing the total nominal Na

Batteries & Supercaps

Research Article
doi.org/10.1002/batt.202500093

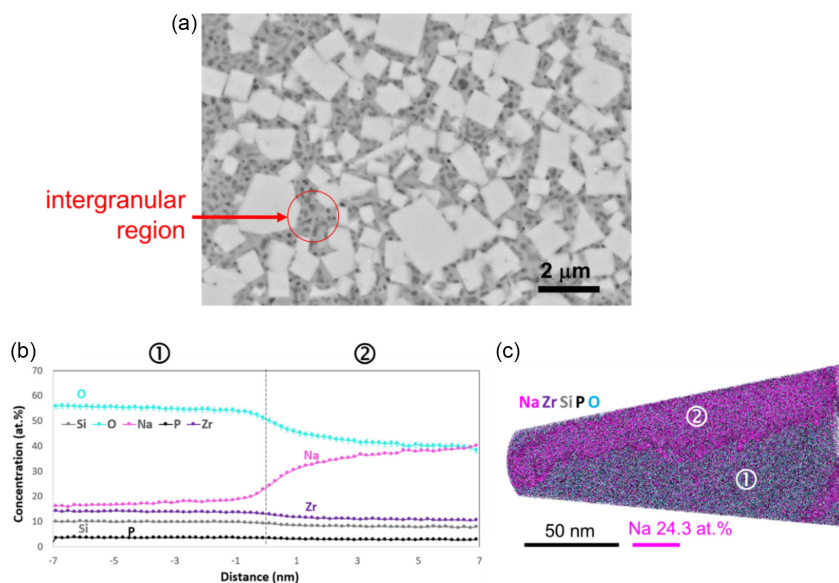**Chemistry Europe**
European Chemical
Societies Publishing

Figure 12. a) High-resolution SEM using BSEs. The red circle highlights the intergranular region containing circular precipitates (dark contrast) characterized by an average lower Z value compared to the surrounding and the brighter grains. b,c) APT results obtained on a $Na_{3.4}Zr_{1.4}Si_{2.6}P_{0.9}O_{11.95}$ (CS2, $x = 0.8$) sample. Proximity histogram (in (b)) constructed with an iso-surface built using a 24.3 at% Na isopleth value. The position 0 nm provides the location of the iso-surface. (c) 3D atom probe map exhibiting the Na redistribution (in pink) in the investigated regions where a Na-rich region (denoted by ②) can be clearly identified.

Table 4. Summary of the quantitative composition (in at%) derived from regions ① and ② shown in Figure 11b, 12b, and S10a–c, Supporting Information.

Sample	Figure	Region	Na	Zr	Si	P	O
$x = 0$	S10a, Supporting Information	①	7.7 ± 0.3	16.5 ± 0.3	11.4 ± 0.3	2.8 ± 0.2	61.2 ± 0.5
Series 1, $x = 0.8$	11	①	10.5 ± 0.3	15.5 ± 0.3	10.6 ± 0.3	3.4 ± 0.2	59.6 ± 0.5
	S10b, Supporting Information	①	12.5 ± 0.3	14.7 ± 0.3	10.3 ± 0.3	3.4 ± 0.2	59.2 ± 0.5
	11	②	20.0 ± 0.3	14 ± 0.3	10.6 ± 0.3	3.4 ± 0.2	52.4 ± 0.5
	S10b, Supporting Information	②	36.2 ± 0.3	11.2 ± 0.3	7.8 ± 0.3	2.6 ± 0.2	42.1 ± 0.5
Series 2, $x = 0.8$	12	①	15.6 ± 0.3	14.2 ± 0.3	10.0 ± 0.3	3.6 ± 0.2	56.6 ± 0.5
	S10c, Supporting Information	①	13.9 ± 0.3	14.3 ± 0.3	10.5 ± 0.3	4.0 ± 0.2	57.4 ± 0.5
	12	②	37.8 ± 0.3	10.8 ± 0.3	8.0 ± 0.3	2.8 ± 0.2	40.6 ± 0.5
	S10c, Supporting Information	②	29.5 ± 0.3	12.1 ± 0.3	9.0 ± 0.3	3.1 ± 0.2	46.4 ± 0.5

composition in NaSICON directly leads to a higher Na content in such elongated cylindrical features.

High-resolution SEM images were acquired on these samples to better understand and localize these Na-rich elongated cylindrical features. Figure 11a and 12a illustrate the sample surface after mechanical polishing. Interestingly, a high fraction of a glassy phase is present in between the NaSICON grains (white areas), where the fraction of this glassy phase is higher for $Na_{3.4}Zr_{1.4}Si_{2.6}P_{0.9}O_{11.95}$ (CS2, $x = 0.8$, Figure 12a) than in $Na_{3.4}Zr_{1.4}Si_{2.2}P_{0.8}O_{10.9}$ (CS1, $x = 0.8$, Figure 11a). Upon careful examination of the intergranular region (highlighted in red in Figure 12a), the presence of nanoprecipitates within the glass matrix can be clearly observed. Whereas the shape of these nanoprecipitates always remains the same (circular from the top view), they vary strongly in terms of depth, especially when compared to those detected by APT in Figure 11c, 12c, and S10b,c, Supporting Information. Moreover, the SEM images were obtained by employing the backscattered electrons

(BSEs), providing Z-contrast information. The nanoprecipitates identified in the intergranular region have a much stronger dark contrast compared with the surrounding, suggesting that these precipitates are enriched in a low-Z element, such as Na. By corroborating these SEM results with the APT, it can be concluded that these nanoprecipitates are, in fact, the Na-rich elongated cylindrical features observed by APT in Figure 11c, 12c, and S10b,c, Supporting Information.

By corroborating the APT and SEM results from Figure 11 and 12 with the conductivity results from Figure 2, one can conclude that the presence of these intergranular regions with Na-rich tubular precipitates reduces the Na ion conductivity at these regions (σ_{ig}) from 3.5×10^{-5} to 5×10^{-6} S cm^{-1}, and the overall ionic conductivity by one order of magnitude. Considering the low ionic conductivity of relevant glasses and their high activation energies (see Table S5, Supporting Information), the decrease of ionic conductivity should be much more pronounced. On the one hand, this is clear proof that the

formation and presence of such a high fraction of glassy phase within the intergranular region is overall detrimental for the NaSICON solid electrolyte due to the amorphous structure which is not adequate for fast Na$^+$ diffusion. On the other hand, the formation of such Na-rich tubular precipitates provides appropriate conductive paths within the intergranular regions being the reason why the ionic conductivity did not decrease as much as it might be expected from the increasing glass fraction.

Another fact that is contrary to the expectations is the low E_a of σ_{ig} (Figure 4b and Table 2) which is lower than E_a of the Na$^+$ ion transport in the NaSICON lattice. In addition, the ^{23}Na MAS NMR spectra revealed a signal that has been assigned to Na_2O_2 filaments corresponding to the Na-rich tubular precipitates observed with APT. Since Na_2O_2 is thermodynamically more stable at room temperature than Na_2O, the interpretation of the NMR results is reasonable, but very likely not the final stadium of transformation of the filaments. For samples exposed to ambient air, it is far more likely that the Na-rich regions absorb water and CO_2[31] leading to hydroxides, hydrates, carbonates, or mixtures thereof. Whereas dry hydroxides have usually low ionic conductivity at room temperature,[50,51] the protonic conductivity of hydrates or water-containing metal organic frameworks (MOFs) is much higher. In addition, the activation energies of hydrates[52] and several MOFs, compiled in recent review articles,[53,54] have very similar values as the data determined here. Therefore, it is likely that the Na-rich tubular regions contribute with proton conduction to the overall ionic conductivity and disguise the low conductivity of the glass regions.

2.3.2. SEM

In a previous publication on these materials,[19] the SEM images of polished cross sections did not show strong differences between the two composition series. For additional topological information on the microstructures, backscattered SEM images of the surface of the sintered bodies were recorded. Surprisingly, the micrographs revealed very substantial differences for the samples with $x = 0.2$ and $x = 0.4$. The surface structure of the samples of CS1 showed a gradual increase of the particle sizes and the glass fraction surrounding the crystalline, nearly cubic NaSICON particles (**Figure 13**). In the case of CS2, the sample with $x = 0.2$ revealed huge, deliquescent particles, indicating liquid-phase sintering. Due to the strong grain growth, many cracks are visible, resulting from the thermal expansion anisotropy of the lattice parameters a and c.[24,55] In the sample with $x = 0.4$, the liquid-phase sintering was reduced and created large and elongated grains, whereas for the two subsequent samples ($x = 0.6$ and $x = 0.8$), the grains again tended to appear as cubes. It should be noted that the two samples with the unusual surface structure were investigated several times and also as fractured cross sections (not shown here). The results were reproducible and the phenomena related to the liquid-phase sintering are restricted to the first few micrometers at the sample surface.

During the second part of the SEM study, the investigation of fracture surfaces and islands of Na_3PO_4 or $Na_3PO_4 \cdot 12H_2O$ (as determined by NMR; in the following summarized as Na_3PO_4) were observed and identified by energy-dispersive
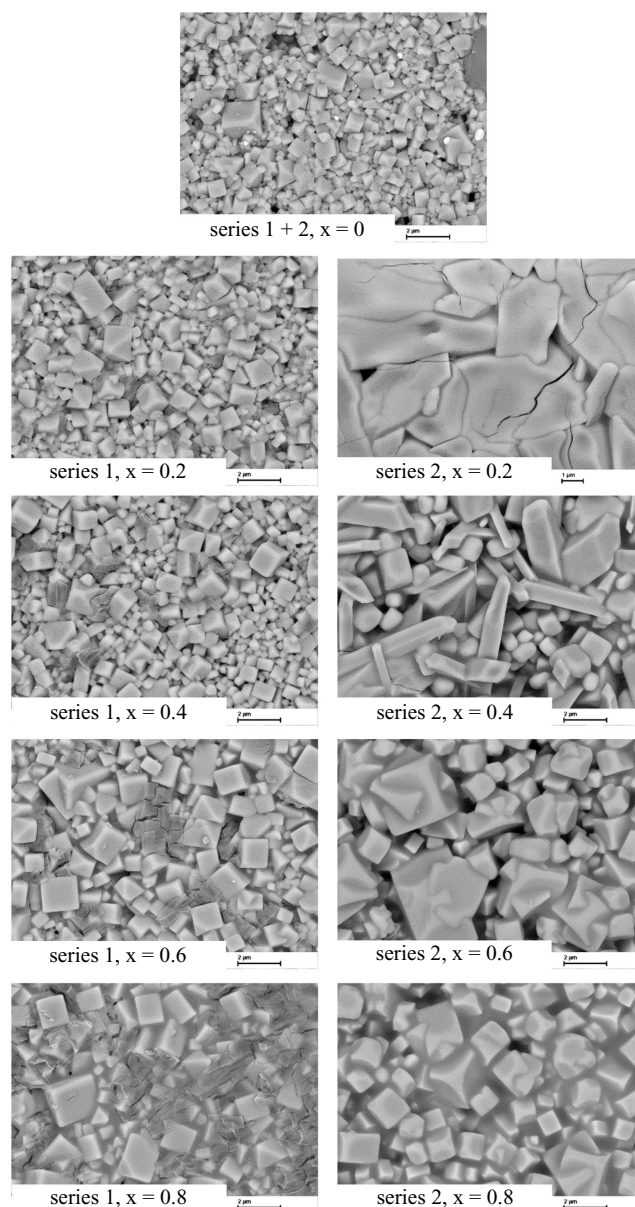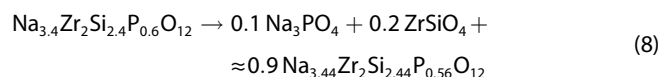

Figure 13. SEM-BSE images of the surface topography of the NaSICON/glass samples in this study.

X-ray spectroscopy (EDX). In previous investigations, these segregations were regarded as inhomogeneities on the sample surface[56] or as reaction products at component interfaces.[57] In the latter case, the appearance of Na_3PO_4 was assumed to result from high interfacial resistance caused by constriction and leading to small local hotspots during current flow. These hotspots induced the decomposition of the NaSICON phase and the formation of Na_3PO_4 as islands at these constriction hotspots. However, the phenomena shown in the following were obtained on samples with the composition $Na_{3.4}Zr_2Si_{2.4}P_{0.6}O_{12}$ that were not exposed to an electrical field and were prepared conventionally by pressing and sintering. Since the images were taken at different times of exposure to ambient air (at relative humidity between 27%-and 32% at 22 °C corresponding to water partial pressures of 7.4 mbar <

Batteries & Supercaps

Research Article
doi.org/10.1002/batt.202500093

Chemistry Europe
European Chemical
Societies Publishing

$p(H_2O) < 8.3$ mbar), the starting point of the time scale was set after sintering, at the point in time at which the samples were taken out of the furnace. The sequence of images shows the same position of a surface fracture. The partially detached ceramic part on the top left of the images was used as a marker to retrieve the same position. For this investigation, the sample was not removed from the sample holder, thus avoiding any mechanical impact and unwanted specimen tilt.

After 1 day of exposure to ambient air, the sample shown (**Figure 14**a) already revealed numerous areas at which Na_3PO_4 was formed (dark grey areas in Figure 14). After three more days of exposure in air (**Figure 14**b), several tiny changes were already visible, which are barely recognizable in the magnification chosen for Figure 14. An example of local changes with a much higher resolution is shown in Figure S11, Supporting Information). When the sample is further exposed for one month ($t = 845$ h), many small dark grey areas are visible, especially on the righthand side of Figure 14c. Until this point, the sequence of figures suggests a slow and continuous decomposition of the NaSICON phase toward Na_3PO_4 according to the tentative chemical equation

$$Na_{3.4}Zr_2Si_{2.4}P_{0.6}O_{12} \rightarrow 0.1\,Na_3PO_4 + 0.2\,ZrSiO_4 + \\ \approx 0.9\,Na_{3.44}Zr_2Si_{2.44}P_{0.56}O_{12} \tag{8}$$

However, zirconium silicate particles could not be clearly detected by EDX and may further decompose to ZrO_2 and SiO_2 (see also Figure S7, Supporting Information). A complete decomposition can be defined as the point at which no

phosphate is left in the NaSICON phase, that is,

$$Na_{3.4}Zr_2Si_{2.4}P_{0.6}O_{12} \rightarrow 0.6\,Na_3PO_4 + 1.2\,ZrSiO_4 + 0.4\,Na_4Zr_2Si_3O_{12} \tag{9}$$
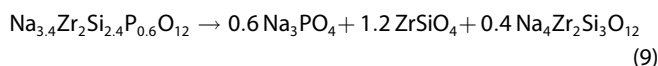
Already in 1987, Warhus et al. established a thermodynamic mixture model with a complete set of thermochemical data for the solid solution $Na_{1+u}Zr_2Si_uP_{3-u}O_{12}$, showing that these compositions are entropy-stabilized.[58] The authors reported a miscibility gap below 330 °C, an important result leading to the decomposition into two NaSICON materials with low and high sodium contents (or silica content). The above reaction equation tends to suggest a decomposition into very stable compounds in the quaternary system Na_2O–P_2O_5–SiO_2–ZrO_2 together with the most stable NaSICON composition.[58] It appears that the decomposition mechanism is different to that which was postulated, but thermodynamic instability can be clearly observed with very slow kinetics.

The often cited "high stability in air" becomes questionable with the changes found here, although the changes may appear only initially at the sample surface. However, considering only some initial days of carelessly leaving samples in the air, this can explain the rather large scatter of ionic conductivity (Figure 2) observed for the samples with the composition $Na_{3.4}Zr_2Si_{2.4}P_{0.6}O_{12}$.

The gradual changes that have occurred up to this point again change in an as-yet inexplicable way when the sample is exposed to air for 10 more days ($t = 1055$ h). The small numerous islands of Na_3PO_4 seem to coalesce into large agglomerates
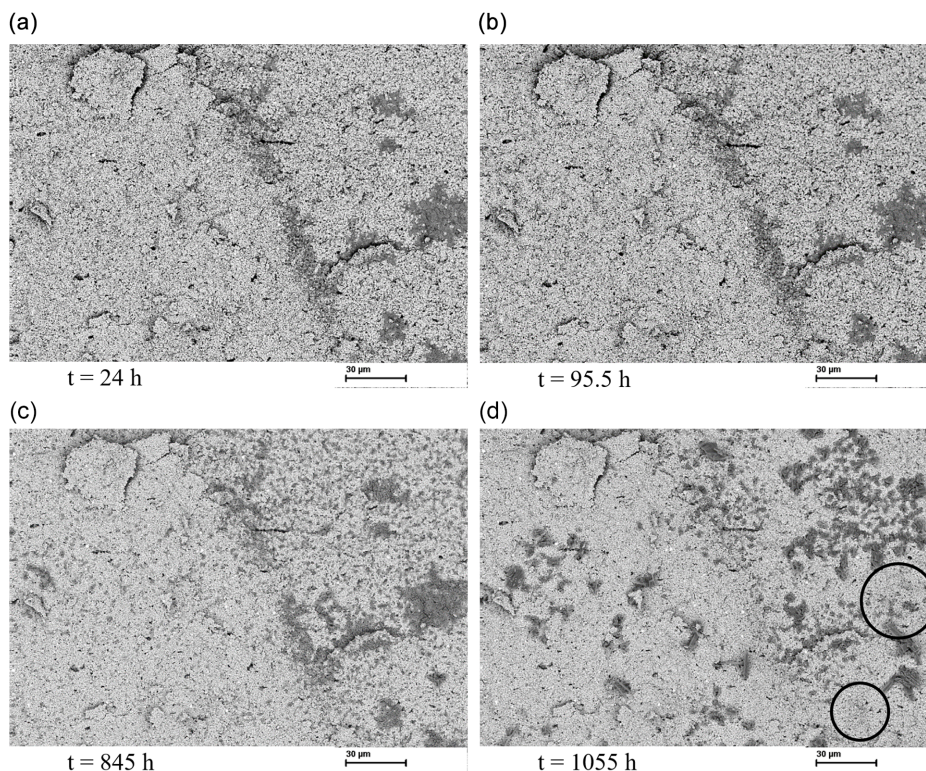

(a) t = 24 h
(b) t = 95.5 h
(c) t = 845 h
(d) t = 1055 h

Figure 14. SEM-BSE images of the same area of a surface fracture of $Na_{3.4}Zr_2Si_{2.4}P_{0.6}O_{12}$ after different times of exposure in ambient air, a–d). Na_3PO_4 is visible as dark grey regions in the micrographs. The circles in (d) show areas in which the previously present Na_3PO_4 disappeared.

Batteries & Supercaps

Research Article
doi.org/10.1002/batt.202500093

Chemistry Europe
European Chemical
Societies Publishing

and, surprisingly, disappear again at other places. This is impressively demonstrated by the large splats on the righthand edge and at the bottom edge of Figure 14d (see circles). Since we have not observed such serious microstructural changes in such short time intervals in any other material, we would be grateful for suggestions to help us better understand these observations.

A faint hint of an explanation may be given by a sample that showed a large crack directly after sintering (see Figure S12, Supporting Information). After 1013 h of exposure in ambient air, only very few Na_3PO_4 spots are visible in the vicinity along the crack, whereas a veritable network of Na_3PO_4 particles was formed at a distance of about 200 μm from the crack. This may suggest a pressure- or stress-related phase transition. Since the crack is obviously a stress-induced artifact of the sample preparation, it may also lead to stress relaxations along the crack. Wherever stress is still above a certain threshold, there seems to be an enhanced formation of Na_3PO_4 particles. Far more work is necessary to better understand the observed phenomena, especially experiments with varying pressures, compositions, and processing conditions.

3. Conclusions

The ionic and thermal transport of materials in the $Na_{3.4}Zr_{2-3x/4}Si_{2.4-x/4}P_{0.6+x/4}O_{12-11x/8}$ and $Na_{3.4}Zr_{2-3x/4}Si_{2.4+x/4}P_{0.6+1.5x/4}O_{12-x/16}$ series show a clear impact on the increasing amount of glass phase with increasing x. σ_{bulk}, which is determined by impedance spectroscopy, and σ_{NMR}, which is derived from NMR relaxometry, are in good agreement, showing values between 1.4 and 6.6 mS cm^{-1}. While the dependence on x is almost constant, the correlation with the real Na^+ content in the conduction paths confirms a maximum conductivity at about 3.4–3.5 mol Na^+/per formula unit, which was previously determined on nearly glass-free NaSICONs. σ_{total} showed a decrease by one order of magnitude with increasing glass fraction. σ_{ig} did not reflect the low conductivity of sodium silicate glasses. Moreover, the values of $E_a(\sigma_{ig})$ are 1) lower than the activation energy of the conductivity of sodium silicate glasses and 2) even lower than $E_a(\sigma_{total})$. This suggests that a different conduction mechanism may be involved and that the observed nm-sized pores in the glass regions may contribute in the form of surface diffusion or proton conduction. In fact, APT showed that the stoichiometry in the samples is not homogenous throughout the whole sample and revealed elongated Na_xO_y precipitates within the glassy phases formed in the intergranular regions of Na-rich NaSICON compounds. Thermal conductivity showed a clear trend toward lower values with higher glass fractions, especially at elevated temperatures.

SEM investigations of the surface of the sintered ceramics found two samples with abnormally large grain growth due to liquid-phase sintering, leading to many cracks induced by thermal expansion anisotropy. Much more concerning were the observations during longer exposure times of a $Na_{3.4}Zr_2Si_{2.4}P_{0.6}O_{12}$ sample to ambient air. Up to about 850 h, an increasing formation of Na_3PO_4 was observed, showing that NaSICON can slowly decompose even at room temperature. A completely unexpected observation after 1055 h was an almost

complete reorganization of the Na_3PO_4 precipitates, which requires further investigation and explanation.

The SEM investigations clearly show that ceramic samples should not be stored in ambient air for long periods and should remain in a glove box or drying room until further use.

The chemical properties described previously[19] and the physical properties reported here lead to several practical implications for the processing of NaSICON ceramics and their application in sodium batteries and other electrochemical devices. The frequently observed formation of small amounts of ZrO_2 in stoichiometric NaSICON compositions, independent on the synthesis method[59] or the starting materials,[60] is also observed here in the sample with $x = 0$.[19] However, samples with $x > 0.1$ do not contain ZrO_2 particles[13,19] and have very low glass fractions. In combination with the fact that compositions with Zr-deficiency of $x \leq 0.4$ have nearly the same total conductivity, in the region of $0.1 < x < 0.25$, phase-pure NaSICON materials with high conductivity and crystallinity can be produced. However, a NaSICON material with very high fraction of crystalline phase is not necessarily the best choice, because with conventional sintering, the ceramic tends to large grain growth resulting in microcrack formation and deterioration of ionic conductivity. For mitigating this mechanical failure mechanism, a low amount of glass phase (for compositions with $0.2 < x < 0.4$) may compensate the stress formation during cooling from high temperatures. A higher glass content may help even more, but it also means that the sintered bodies stick to any material and cannot be used any further—unless the intention is to produce a composite material in this way.

4. Experimental Section

Different powders within the two composition series with $x = 0$, 0.2, 0.4, 0.6, and 0.8 were synthesized by the solution-assisted solid-state reaction, as described elsewhere.[59,61] The dried reaction products were calcined at 800 °C for 3 h to form an amorphous raw powder. The calcined powders were then ball-milled in ethanol with zirconia balls on a roller bench for four days. After drying, the powders were pressed into pellets (diameter = 13 mm, thickness ≈ 2 mm) applying a pressure of about 150 MPa followed by sintering at 1250 °C for 4 h on a Pt foil. For the conductivity measurements, pellets were also sintered at various temperatures between 1030 and 1250 °C in steps of 20 K. After sintering, the experimental density was obtained geometrically considering the phase fraction of the glass.[19] Unless mentioned otherwise, the samples sintered at 1250 °C were used for consistent comparison among the compositions and the different investigation methods.

For ionic conductivity measurements, the surfaces of sintered pellets were dry polished using SiC sandpapers up to a grit of 4000 and then sputter-coated with gold on each side as blocking electrodes using a Cressington 108 coater. The ionic conductivity was measured at different temperatures between −100 and 100 °C in a temperature-controlled chamber (Novocontrol Technologies BDS1100). Two commercial electrochemical systems (Keysight E4991B and Novocontrol Technologies Alpha-A) with an AC frequency range from 3 GHz to 1 MHz and from 3 MHz to 1 Hz were applied for impedance measurements, respectively. An alternating voltage amplitude of ±10 mV was used during measurements. The resulting impedance spectra were fitted using the software "Z-view" (Scribner Associates Inc). The powders and pellets were stored in an argon-filled glove box until used later for further investigations.

Batteries & Supercaps

Research Article
doi.org/10.1002/batt.202500093

Chemistry Europe
European Chemical
Societies Publishing

Thermal conductivities were determined from thermal diffusivity measurements using the light-flash analyzer LFA-467 (Netzsch–Gerätebau GmbH). Prior to measurement, the samples were spray-coated with graphite to enhance light absorption and infrared emission. Below room temperature, diffusivities were measured using a mercury cadmium telluride detector and a ZnS furnace window; above room temperature, an InSb detector and a sapphire furnace window were used. The measurement software optimized the detection time automatically during measurement. The raw data were fitted with an improved Cape–Lehmann model.[63,64] At each temperature, thermal diffusivity was measured three times and the average used for further analysis. The thermal conductivity, κ, is the product of thermal diffusivity, D, specific isobaric heat capacity, c_p, and density, ρ:

$$\kappa = D \cdot c_p \cdot \rho \tag{10}$$

The heat capacity was interpolated between literature values[48] for $NaZr_2P_3O_{12}$ and $Na_4Zr_2Si_3O_{12}$ based on the sodium content of the sample. For each composition, three samples were investigated and the arithmetic mean taken as the data value and the standard deviation as uncertainty.

NMR measurements were carried out to analyze the local environment of different cations and the transport properties of Na^+ ions. Static, temperature-dependent ^{23}Na NMR spectra and T_1 relaxation time measurements were performed on a Bruker Avance neo 200 MHz spectrometer with a magnetic field strength of 4.7 T. The samples were measured in NMR quartz glass tubes at ambient atmosphere. For the data acquisition, a solid-echo and inversion-recovery sequence was used. The recycle delay was always well above five times T_1. 1 M NaCl was used as the chemical shift reference. 29Si and ^{31}P MAS spectra were acquired on a Bruker Avance 500 MHz spectrometer with a magnetic field strength of 11.7 T. The samples were filled in a 2.5 mm rotor and a rotation frequency of 30 and 25 kHz was used for ^{29}Si and ^{31}P, respectively. The recycle delay and $\pi/2$-pulse length were set to 60 s and 1.8 μs for ^{29}Si and to 30 s and 3.2 μs for ^{31}P, respectively. ^{23}Na MAS NMR spectra were detected on a Bruker Avance 600 MHz spectrometer with a magnetic field strength of 14.7 T. The samples were filled in a 2.5 mm rotor, and a rotation frequency of 20 kHz was used. The recycle delay and $\pi/2$-pulse length were set to 15 s and 3.0 μs, respectively. The spectra were referenced with tetramethylsilane for ^{29}Si, H_3PO_4 (85%) for ^{31}P, and 1 M NaCl for ^{23}Na.

APT[64] is one of the few tools available that allows the quantification of light alkalis, such as Li and Na, down to the atomic level and in three dimensions. Although APT has been widely used in the past for the analysis of various semiconducting[65] and insulating[66] materials, it remains challenging to use for some very soft or beam-sensitive materials,[67,68] as is the case for battery materials.[69] However, using appropriate parameters,[70] it is possible to accurately investigate the Li^+ redistribution down to the interface level and in three dimensions. The same parameters, namely a base temperature of 40 K, laser pulse energy of 10 pJ, and pulse frequency of 250 kHz, were used to investigate the Na^+ redistribution in the $Na_{3.4}Zr_{2-3x/4}Si_{2.4-x/4}P_{0.6+x/4}O_{12-11x/8}$ and $Na_{3.4}Zr_{2-3x/4}Si_{2.4+x/4}P_{0.6+1.5x/4}O_{12-x/16}$ series. The selected parameters aim at reducing the temperature increase on the needle-shaped specimens, preventing Na from being artificially redistributed on the apex of the tip during APT experiments, as observed with Li.[70] Moreover, the needle-shaped specimens required for the APT experiments were prepared using only low energetic Ga^+ ions from the focused ion beam system, specifically 8 kV and 50 pA. These APT tips were then cleaned in an additional step to remove any amorphization or Ga contamination using 2 kV and 23 pA.

The microstructure of the sintered pellets was examined by SEM with a GeminiSEM 450 ZEISS scanning electron microscope (Carl Zeiss Microscopy GmbH, Oberkochen, Germany). The surface structure of the samples was investigated and the fractured surfaces were analyzed with a special focus on inhomogeneities in the samples. The images were taken with a BSE detector with an acceleration voltage of 8 kV and a current of 1 nA. For the elemental distribution, an ULTIM MAX 170 energy-dispersive spectrometer from Oxford Instruments was used. The low voltage was applied in order to avoid beam damage during scanning. Additionally, focusing of the image was always made in one place, and then the sample was immediately moved to another nearby area to take the image with a slow scan rate. By doing so, beam damage, resulting in surface cracks for example, could be strongly minimized.

Acknowledgements

Conflict of Interest

The authors declare no conflict of interest.

Author Contributions

Frank Tietz: conceptualization (lead); formal analysis (lead); funding acquisition (supporting); supervision (lead); visualization (lead); writing—original draft (lead); writing—review & editing (lead). **Philipp Odenwald**: data curation (equal); investigation (equal). **Doris Sebold**: data curation (equal); investigation (equal). **Mareen Schaller**: data curation (equal); investigation (equal); visualization (equal); writing—review & editing (equal). **Thorben Böger**: data curation (equal); investigation (equal); writing—review & editing (supporting). **Jan Köttgen**: data curation (supporting); investigation (equal); visualization (equal). **Qianli Ma**: data curation (equal); formal analysis (equal); investigation (equal); writing—review & editing (supporting). **Sylvio Indris**: formal analysis (equal); investigation (supporting); writing—review & editing (equal). **Wolfgang G. Zeier**: formal analysis (equal); funding acquisition (lead); investigation (supporting); writing—review & editing (supporting). **Oana Cojocaru-Miredin**: formal analysis (equal); investigation (equal); supervision (equal); writing—review & editing (equal). **Dina Fattakhova-Rohlfing**: formal analysis (supporting); funding acquisition (lead); project administration (equal); supervision (equal); writing—review & editing (equal).

Batteries & Supercaps

Research Article
doi.org/10.1002/batt.202500093

Chemistry Europe
European Chemical
Societies Publishing

[1] T. Oshima, M. Kajita, A. Okuno, *Int. J. Appl. Ceram. Technol.* **2004**, *1*, 269.
[2] R. Benato, N. Cosciani, G. Crugnola, S. Dambone Sessa, G. Lodi, C. Parmeggiani, M. Todeschini, *J. Power Sources* **2015**, *293*, 127.
[3] J. B. Goodenough, H.-Y. P. Hong, J. Kafalas, *Mater. Res. Bull.* **1976**, *11*, 203.
[4] H.-Y. P. Hong, *Mater. Res. Bull.* **1976**, *11*, 173.
[5] U. von Alpen, M. F. Bell, H. H. Höfer, *Solid State Ionics* **1981**, *3*, 215.
[6] J. Engell, S. Mortensen, L. Møller, *Solid State Ionics* **1983**, *9*, 877.
[7] S. Yde-Andersen, J. S. Lundgaard, L. Møller, J. Engell, *Solid State Ionics* **1984**, *14*, 73.
[8] A. K. Kuriakose, T. A. Wheat, A. Ahmad, J. Dirocco, *J. Am. Ceram. Soc.* **1984**, *67*, 179.
[9] H. Perthuis, P. Colomban, *Ceram. Int.* **1986**, *12*, 39.
[10] W. Go, J. Kim, J. Pyo, J. B. Wolfenstine, Y. Kim, *ACS Appl. Mater. Interfaces* **2021**, *13*, 52727.
[11] O. Bohnke, S. Ronchetti, D. Mazza, *Solid State Ionics* **1999**, *122*, 127.
[12] E. Traversa, H. Aono, Y. Sadaoka, L. Montanaro, *Sens. Actuators, B* **2000**, *65*, 204.
[13] A. J. Kang Tieu, E. Mahayoni, Y. Li, Z. Deng, F. Fauth, J.-N. Chotard, V. Seznec, S. Adams, Ch Masquelier, P. Canepa, *J. Mater. Chem. A* **2023**, *11*, 23233.
[14] S. Susman, C. J. Delbecq, J. A. McMillan, M. F. Roche, *Solid State Ionics* **1983**, *9*, 667.
[15] A. Niyompan, D. Holland, *J. Non-Cryst. Solids* **2001**, *293–295*, 709.
[16] J. A. S. Oh, L. He, A. Plewa, M. Morita, Y. Zhao, T. Sakamoto, X. Song, W. Zhai, K. Zeng, L. Lu, *ACS Appl. Mater. Interfaces* **2019**, *11*, 40125.
[17] H. Wang, G. Zhao, S. Wang, D. Liu, Z. Mei, Q. An, J. Jiang, H. Guo, *Nanoscale* **2022**, *14*, 823.
[18] B. Santhoshkumar, M. B. Choudhary, A. K. Bera, S. M. Yusuf, M. Ghosh, B. Pahari, *J. Am. Ceram. Soc.* **2022**, *105*, 5011.
[19] E. Dashjav, M.-T. Gerhards, F. Klein, D. Grüner, T. C. Hansen, J. Rohrer, K. Albe, F. Fattakhova-Rohlfing, F. Tietz, *Next Energy* **2024**, *4*, 100130.
[20] S. M. Haile, G. Staneff, K. H. Ryu, *J. Mater. Sci.* **2001**, *36*, 1149.
[21] S. M. Haile, D. L. West, J. Campbell, *J. Mater. Res.* **1998**, *13*, 1576.
[22] D. S. McLachlan, *J. Phys. C: Solid State Phys.* **1987**, *20*, 865.
[23] D. S. McLachlan, M. Blaszkiewicz, R. E. Newnham, *J. Am. Ceram. Soc.* **1990**, *73*, 2187.
[24] Q. Ma, C.-L. Tsai, X.-K. Wei, M. Heggen, F. Tietz, J. Irvine, *J. Mater. Chem. A* **2019**, *7*, 7766.
[25] U. von Alpen, M. F. Bell, H. H. Höfer, *Solid State Ionics* **1982**, *7*, 345.
[26] H.-B. Kang, N.-H. Cho, *J. Mater. Sci.* **1999**, *34*, 5005.
[27] A. Clearfield, M. A. Subramanian, W. Wang, P. Jerus, *Solid State Ionics* **1983**, *9*, 895.
[28] W. H. Baur, J. R. Dygas, D. H. Whitmore, J. Faber, *Solid State Ionics* **1986**, *18*, 935.
[29] S. Naqash, F. Tietz, E. Yazhenskikh, M. Müller, O. Guillon, *Solid State Ionics* **2019**, *336*, 57.
[30] A. Loutati, Y. J. Sohn, F. Tietz, *ChemPhysChem* **2021**, *22*, 995.
[31] M. Guin, S. Indris, M. Kaus, H. Ehrenberg, F. Tietz, O. Guillon, *Solid State Ionics* **2017**, *302*, 102.
[32] H. Maekawa, T. Maekawa, K. Kawamura, T. Yokokawa, *J. Non-Cryst. Solids* **1991**, *127*, 53.
[33] P. Raghavan, *At. Data Nucl. Tables* **1989**, *42*, 189.
[34] H. Yamashita, H. Yoshino, K. Nagata, I. Yamaguchi, M. Ookawa, T. Maekada, *J. Ceram. Soc. Jpn.* **1998**, *106*, 539.
[35] K. J. D. Mackenzie, M. E. Smith, *Multinuclear Solid-State NMR of Inorganic Materials*, Elsevier Science Ltd., Oxford **2002**, ISBN: 9780080437873.
[36] G. L. Turner, K. A. Smith, R. J. Kirkpatrick, E. Oldfield, *J. Magn. Reson.* **1986**, *70*, 408.
[37] M. Witschas, H. Ecker, *J. Phys. Chem. A* **1999**, *103*, 10764.
[38] T. J. Bastow, *Z. Naturforsch.,* **1994**, *49*, 320.
[39] H. Bloembergen, E. M. Purcell, R. V. Pound, *Phys. Rev.* **1948**, *73*, 679.
[40] P. Heitjans, S. Indris, *J. Phys.: Condens. Matter* **2003**, *15*, R1257.
[41] A. Einstein, *Ann. Phys.* **1905**, *322*, 549.
[42] M. von Smoluchowski, *Ann. Phys.* **1906**, *326*, 756.
[43] S. Hunklinger, C. Enss, *Solid State Physics*, De Gruyter, Berlin, Boston **2022**, https://doi.org/10.1515/9783110666502.
[44] Z. Cheng, B. Zahiri, X. Ji, C. Chen, D. Chalise, P. V. Braun, D. G. Cahill, *Small* **2021**, *17*, e2101693.
[45] T. Böger, T. Bernges, Y. Li, P. Canepa, W. G. Zeier, *ACS Appl. Energy Mater.* **2023**, *6*, 10704.

[46] J. Neises, W. S. Scheld, A.-R. Seok, S. Lobe, M. Finsterbusch, S. Uhlenbruck, R. Schmechel, N. Benson, *J. Mater. Chem. A* **2022**, *10*, 12177.
[47] M. Rohde, I. U. I. Mohsin, C. Ziebert, H. J. Seifert, *Int. J. Thermophys.* **2021**, *42*, 136.
[48] Th Böger, T. Bernges, M. T. Agne, P. Canepa, F. Tietz, W. G. Zeier, *J. Am. Chem. Soc.* **2024**, *146*, 32678.
[49] J. Keutgen, A. J. London, O. Cojocaru-Mirédin, *Microsc. Microanal.* **2021**, *27*, 28.
[50] Y. M. Baikov, *Sov. Electrochem.* **1982**, *18*, 1256.
[51] K.-H. Haas, U. Schindewolf, *J. Solid State Chem.* **1984**, *54*, 342.
[52] U. Chowdhry, J. R. Barkley, A. D. English, A. W. Sleight, *Mat. Res. Bull.* **1982**, *17*, 917.
[53] P. Ramaswamy, N. E. Wong, G. K. H. Shimizu, *Chem. Soc. Rev.* **2014**, *43*, 5913.
[54] Y. Ye, L. Gong, S. Xiang, Z. Zhang, B. Chen, *Adv. Mater.* **2020**, *32*, 1907090.
[55] F. Tietz, *Sodium-Ion Batteries. Materials, Characterization, and Technology*, Vol. *2* (Eds: M. Titirici, P. Adelhelm, Y. Hu), Wiley-VCH, Weinheim, Germany **2022**, pp. 391–428, Ch. 13, https://doi.org/10.1002/9783527825769.ch13.
[56] E. Quérel, I. D. Seymour, A. Cavallaro, Q. Ma, F. Tietz, A. Aguadero, *J. Phys. Energy* **2021**, *3*, 044007.
[57] L. E. Goodwin, P. Till, M. Bhardwaj, N. Nazer, P. Adelhelm, F. Tietz, W. G. Zeier, F. H. Richter, J. Janek, *ACS Appl. Mater. Interfaces* **2023**, *5*, 50457.
[58] U. Warhus, J. Maier, A. Rabenau, *J. Solid State Chem.* **1988**, *72*, 113.
[59] S. Naqash, Q. Ma, F. Tietz, O. Guillon, *Solid State Ionics* **2017**, *302*, 83.
[60] Y. Li, Z. Sun, C. Sun, H. Jin, Y. Zhao, *Ceram. Int.* **2023**, *49*, 3094.
[61] Q. Ma, M. Guin, S. Naqash, C.-L. Tsai, F. Tietz, O. Guillon, *Chem. Mater.* **2016**, *28*, 4821.
[62] J. Blumm, J. Opfermann, *High Temp.-High Press.* **2002**, *34*, 515.
[63] J. A. Cape, G. W. Lehman, *J. Appl. Phys.* **1963**, *34*, 1909.
[64] B. Gault, A. Chiaramonti, O. Cojocaru-Mirédin, P. Stender, R. Dubosq, Ch Freysoldt, S. Kumar Makineni, T. Li, M. Moody, J. M. Cairney, *Nat. Rev. Methods Primers* **2021**, *1*, 51.
[65] a) O. Cojocaru-Mirédin, L. Abdellaoui, M. Nagli, S. Zhang, Y. Yu, Ch. Scheu, D. Raabe, M. Wuttig, Y. Amouyal, *ACS Appl. Mater. Interfaces* **2017**, *9*, 14779; b) O. Cojocaru-Mirédin, T. Schwarz, D. Abou-Ras, *Scr. Mater.* **2018**, *148*, 106; c) O. Cojocaru-Mirédin, H. Hollermann, A. M. Mio, A. Y. T. Wang, M. Wuttig, *J. Phys.: Condens. Matter* **2019**, *31*, 204002; d) O. Cojocaru-Mirédin, M. Raghuwanshi, R. Wuerz, S. Sadewasser, *Adv. Funct. Mater.* **2021**, *31*, 2103119.
[66] a) K. Stiller, L. Viskari, G. Sundell, F. Liu, M. Thuvander, H.-O. Andrén, D. J. Larson, T. Prosa, D. Reinhard, *Oxid. Met.* **2013**, *79*, 227; b) J. Perrin Toinin, C. Hatzoglou, J. Voronkoff, H. Montigaud, D. Guimard, M. Wuttig, F. Vurpillot, O. Cojocaru-Mirédin, *Adv. Mater. Technol.* **2023**, *8*, 2200922.
[67] N. A. Rivas, A. Babayigit, B. Conings, T. Schwarz, A. Sturm, A. Garzón Manjón, O. Cojocaru-Mirédin, B. Gault, F. U. Renner, *PLoS One* **2020**, *15*, 1.
[68] S. Caicedo-Dávila, H. Funk, R. Lovrinčić, Ch Müller, M. Sendner, O. Cojocaru-Mirédin, F. Lehmann, R. Gunder, A. Franz, S. Levcenco, A. V. Cohen, L. Kronik, B. Haas, C. T. Koch, D. Abou-Ras, *J. Phys. Chem. C* **2019**, *123*, 17666.
[69] a) P. Parikh, H. Chung, E. Vo, A. Banerjee, Y. S. Meng, A. Devaraj, *J. Phys. Chem. C* **2022**, *126*, 14380; b) O. Cojocaru-Mirédin, A. Devaraj, *MRS Bull.* **2022**, *47*, 680; c) S. Stegmaier, R. Schierholz, I. Povstugar, J. Barthel, S. P. Rittmeyer, S. Yu, S. Wengert, S. Rostami, H. Kungl, K. Reuter, R.-A. Eichel, C. Scheurer, *Adv. Energy Mater.* **2021**, *11*, 2100707; d) M. P. Singh, E. V. Woods, S.-H. Kim, C. Jung, L. S. Aota, B. Gault, *Batteries Supercaps* **2024**, *7*, e202300403; e) S.-H. Kim, S. Antonov, X. Zhou, L. T. Stephenson, C. Jung, A. A. El-Zoka, D. K. Schreiber, M. Conroy, B. Gault, *J. Mater. Chem. A* **2022**, *10*, 4926.
[70] O. Cojocaru-Mirédin, J. Schmieg, M. Müller, A. Weber, E. Ivers-Tiffée, D. Gerthsen, *J. Power Sources* **2022**, *539*, 231417.